An optimal scheme for top quark mass measurement near the $t\bar{t}$ threshold at future e^+e^- colliders*

Wei-Guo Chen(陈卫国)[1] Xia Wan(万霞)[2] You-Kai Wang(王由凯)[3]
School of Physics & Information Technology, Shaanxi Normal University, Xi'an 710119, China

Abstract: A top quark mass measurement scheme near the $t\bar{t}$ production threshold in future e^+e^- colliders, e.g. the Circular Electron Positron Collider (CEPC), is simulated. A χ^2 fitting method is adopted to determine the number of energy points to be taken and their locations. Our results show that the optimal energy point is located near the largest slope of the cross section v. beam energy plot, and the most efficient scheme is to concentrate all luminosity on this single energy point in the case of one-parameter top mass fitting. This suggests that the so-called data-driven method could be the best choice for future real experimental measurements. Conveniently, the top mass statistical uncertainty can also be calculated directly by the error matrix even without any sampling and fitting. The agreement of the above two optimization methods has been checked. Our conclusion is that by taking 50 fb^{-1} total effective integrated luminosity data, the statistical uncertainty of the top potential subtracted mass can be suppressed to about 7 MeV and the total uncertainty is about 30 MeV. This precision will help to identify the stability of the electroweak vacuum at the Planck scale.

Keywords: CEPC, top mass, threshold scan

PACS: 14.65.Ha **DOI:** 10.1088/1674-1137/42/5/053002

1 Introduction

The Higgs potential is closely related to both the Higgs boson mass and the top quark pole mass. Especially, if the top quark mass is too heavy, the quartic Higgs coupling λ in the Standard Model may be negative at large energy scale before the Planck scale and the stability of electroweak vacuum breaks. Therefore, the determination of the electroweak vacuum stability needs precise measurements of both the Higgs boson mass and the top quark mass. At the Large Hadron Collider (LHC), the Higgs mass is measured with a precision of $\mathcal{O}(200)$ MeV [1], which means, currently, the electroweak vacuum stability is more sensitive to the uncertainty of the top quark pole mass.

Before detailed investigation of the top quark mass, one should keep in mind that the top quark mass is not a direct experimental observable. This means the value of the experimental output mass depends on the theoretical input definitions.

Theoretically, several kinds of top mass can be defined.

1) Pole mass

The pole mass has an inherent ambiguity of the order of $\mathcal{O}(\Lambda_{\rm QCD})$ [2–4] and leads to an instability of top threshold peak location at different orders. The pole mass is therefore not a good definition for experimental measurements and unambiguous definitions of top mass are necessary. The top quark propagator is expressed as

$$D(\not{p})=\frac{i}{\not{p}-m_0-\sum_0(\not{p})}=\frac{i}{\not{p}-m_{\rm R}-\sum_{\rm R}(\not{p})}. \quad (1)$$

From the denominator, we have

$$m_{\rm pole}=m_0+\sum_0(\not{p})=m_{\rm R}+\sum_{\rm R}(\not{p}), \quad (2)$$

where $m_0/m_{\rm R}$ is the bare/renormalized top mass, and $\sum_0(\not{p})/\sum_{\rm R}(\not{p})$ is the unrenormalized/renormalized top quark self-energy contribution. The ultraviolet divergence of $\sum_0^{(1)}(\not{p})$ should be absorbed by the bare mass and its infrared (IR) part has the form

$$\sum_0^{(1)}(\not{p})\to-\frac{1}{2}\int_\Lambda\frac{{\rm d}^3\vec{q}}{(2\pi)^3}\frac{4\pi C_{\rm F}\alpha_{\rm s}(q)}{\vec{q}^2}, \quad (3)$$

Received 5 January 2018, Revised 4 March 2018, Published online 20 April 2018

∗ Supported by National Science Foundation of China (11405102) and the Fundamental Research Funds for the Central Universities of China (GK201603027, GK201803019)

1) E-mail: chenwg19910708@snnu.edu.cn

2) E-mail: wanxia@snnu.edu.cn

3) E-mail: wangyk@snnu.edu.cn

where Λ is the lower bound of the loop momentum q and $C_{\rm F}=4/3$. Considering the RGE running of $\alpha_{\rm s}$ from the loop momentum scale q to $m_{\rm R}$ [5],

$$\begin{aligned}\alpha_{\rm s}(q) &= \frac{1}{b_0\ln(q^2/\Lambda^2)}=\frac{\alpha_{\rm s}(m_{\rm R})}{1-\alpha_{\rm s}(m_{\rm R})b_0\ln(m_{\rm R}^2/q^2)}\\ &= \sum_{n=0}^{\infty}\alpha_{\rm s}^{n+1}(m_{\rm R})b_0^n\ln^n\frac{m_{\rm R}^2}{q^2}.\end{aligned} \tag{4}$$

and

$$\int_o^{m_{\rm R}}{\rm d}q\ln^n\frac{m_{\rm R}^2}{q^2}=m_{\rm R}2^n\int_0^1{\rm d}x\ln^n\frac{1}{x}=m_{\rm R}2^n n!, \tag{5}$$

the pole mass can be expressed as

$$m_{\rm pole}=m_{\rm R}\left(1+\sum_{n=0}^{\infty}c_n\alpha_{\rm s}^{n+1}(m_{\rm R})\right), \tag{6}$$

where the coefficient $c_n\to 2^n n!$ and the convergence of perturbative expansion breaks when $n\to\infty$. The behavior of this IR renormalon results in an intrinsic ambiguity of the pole mass. The ambiguity is estimated as [4]

$$\delta m_{\rm pole}=\frac{C_{\rm F}}{2N_{\rm f}|\beta_0|}{\rm e}^{-C/2}\Lambda_{\rm QCD}\left(\ln\frac{m^2}{\Lambda_{\rm QCD}^2}\right)^{\beta_1/(2\beta_0^2)}\sim\Lambda_{\rm QCD}, \tag{7}$$

where β_i is the $i+1$th-loop beta function, and C is a constant related to renormalization scheme.

To avoid the pole mass ambiguity, several short distance masses can be defined due to the IR-sensitive term cancellation between the pole mass and the static potential $V(r)$ of toponium.

2) Potential subtracted (PS) mass

From conservation of the total energy, we have

$$2m_{\rm pole}+V(r)=2m_{\rm PS}+V(r,\mu_{\rm f}), \tag{8}$$

where $V(r,\mu_{\rm f})$ is the subtracted potential and can be defined as [6]

$$V(r,\mu_{\rm f})=V(r)-\int_{|\vec{q}|<\mu_{\rm f}}\frac{{\rm d}^3\vec{q}}{(2\pi)^3}\tilde{V}(\vec{q}). \tag{9}$$

At $\alpha_{\rm s}$ leading order, $\tilde{V}(\vec{q})=-\dfrac{4\pi C_{\rm F}\alpha_{\rm s}(\mu)}{\vec{q}^2}$ is the potential in momentum space. So the relations between different masses are

$$\begin{aligned}m_{\rm PS}&=\frac{1}{2}[2m_{\rm pole}+V(r)-V(r,\mu_{\rm f})]\\ &=m_{\rm pole}+\frac{1}{2}\int_{|\vec{q}|<\mu_{\rm f}}\frac{{\rm d}^3\vec{q}}{(2\pi)^3}\tilde{V}(\vec{q}).\end{aligned} \tag{10}$$

By considering Eqs. (2)and (6), we have

$$\begin{aligned}m_{\rm PS}=&m_{\rm R}\left(1+\sum_{n=0}^{\infty}c_n\alpha_{\rm s}^{n+1}(m_{\rm R})\right)\\ &-\frac{1}{2}\int_{|\vec{q}|<\mu_{\rm f}}\frac{{\rm d}^3\vec{q}}{(2\pi)^3}\frac{4\pi C_{\rm F}\alpha_{\rm s}(\mu)}{q^2}\\ =&m_{\rm R}\left(1+\sum_{n=0}^{\infty}c_n\alpha_{\rm s}^{n+1}(m_{\rm R})\right)-\mu_{\rm f}\sum_{n=0}^{\infty}c_n'\alpha_{\rm s}^{n+1}(m_{\rm R}).\end{aligned} \tag{11}$$

From Eqs. (4) and (5) we see that the coefficients c_n and c_n' have the same divergent form (c_n, $c_n'\to 2^n n!$) as $n\to\infty$ in order for the IR renormalons to be cancelled. Only non-ambiguous terms remain. The remaining coefficient $\mu_{\rm f}$ cannot be removed. This is why the PS mass depends on the scale $\mu_{\rm f}$ when it is expressed by other short-distance masses (such as the $\overline{\rm MS}$ mass).

3) $1S$ mass

The $1S$ mass is defined as half of the perturbative mass of the toponium $1\ ^3S_1$ ground state and is given by [7, 8]

$$m_{1S}=\frac{1}{2}(2m_{\rm pole}+E_{1S}(m_{\rm pole},\alpha_{\rm s}(\mu))), \tag{12}$$

where

$$E_{1S}(m_{\rm pole},\alpha_{\rm s}(\mu))=\int\frac{{\rm d}^3\vec{p}}{(2\pi)^3}\frac{{\rm d}^3\vec{q}}{(2\pi)^3}\tilde{\psi}_{1S}^*(\vec{p})\tilde{H}(\vec{p},\vec{q})\tilde{\psi}_{1S}(\vec{q}), \tag{13}$$

$\tilde{H}(\vec{p},\vec{q})$ and $\tilde{\psi}_{1S}$ are the Hamiltonian and the wave function in the $1\ ^3S_1$ state in momentum space respectively.

Considering the IR behavior,

$$\begin{aligned}E_{1S}^{\rm IR}(m_{\rm pole},\alpha_{\rm s}(\mu))=&\int_{\rm IR}\frac{{\rm d}^3\vec{p}}{(2\pi)^3}\frac{{\rm d}^3\vec{q}}{(2\pi)^3}\tilde{\psi}_{1S}^*(\vec{p})\tilde{H}(\vec{p},\vec{q})\tilde{\psi}_{1S}(\vec{q})\\ =&\int_{\rm IR}\frac{{\rm d}^3\vec{p}}{(2\pi)^3}\frac{{\rm d}^3\vec{q}}{(2\pi)^3}\tilde{\psi}_{1S}^*(\vec{p})\\ &\times\left(\frac{\vec{p}^2}{2m_{\rm pole}}+\frac{\vec{q}^2}{2m_{\rm pole}}+\tilde{V}(\vec{p}-\vec{q})\right)\tilde{\psi}_{1S}(\vec{q}).\end{aligned} \tag{14}$$

Dropping the momentum terms in the Hamiltonian and denoting the IR region $|\vec{q}|,|\vec{p}|<\mu_{\rm f}$,

$$\begin{aligned}E_{1S}^{\rm IR}(m_{\rm pole},\alpha_{\rm s}(\mu))\sim&\int_{\rm IR}\frac{{\rm d}^3\vec{p}}{(2\pi)^3}\frac{{\rm d}^3\vec{q}}{(2\pi)^3}\tilde{\psi}_{1S}^*(\vec{p})\tilde{V}(\vec{p}-\vec{q})\tilde{\psi}_{1S}(\vec{q})\\ \sim&\int_{|\vec{q}|,|\vec{p}|<\mu_{\rm f}}\frac{{\rm d}^3\vec{p}}{(2\pi)^3}\frac{{\rm d}^3\vec{q}}{(2\pi)^3}|\tilde{\psi}_{1S}^*(\vec{p})|^2\tilde{V}(\vec{p}-\vec{q})\\ \sim&\int_{|\vec{q}|<\mu_{\rm f}}\frac{{\rm d}^3\vec{q}}{(2\pi)^3}\tilde{V}(\vec{q}).\end{aligned} \tag{15}$$

We see that it is very like the PS mass case, as the IR behavior of the $E_{1S}(m_{\rm pole},\alpha_{\rm s}(\mu))$ results in an IR renormalon which cancels with the ambiguity of $m_{\rm pole}$. Thus the $1S$ mass is non-ambiguous.

4) $\overline{\rm MS}$ mass: defined by the modified minimal subtraction renormalization scheme.

Experimentally, the top quark mass can be measured mainly by two methods. The first method is from the reconstruction of top decay products [9]. For example, the current most precise top mass is obtained from the lepton+jets channel. The main source of errors comes from the jet energy scale calibration. However, the experimentally measured top mass corresponds to none of the above theoretical mass definitions. This problem has been well discussed in a recent study [5], in which three arguments are listed. Firstly, the top mass derived from kinematical reconstruction does not correspond to a well defined mass from perturbation theory. Secondly, jets from top decay have non-perturbative effects. Thirdly, parton shower models in Monte Carlo have irreducible non-perturbative error. To have a clear distinction, the experimentally measured top mass from decay product reconstruction is usually named the MC mass. As an approximation, sometimes people do not distinguish the MC mass and the pole mass, as their difference is estimated to be less than 1 GeV.

The second method is to extract the top mass from the measured $\rm t\bar{t}$ cross section by comparing it with the theoretical cross section [10–13]. The two cross section curves have different dependent relations on the fictional top mass and the overlap region corresponds to the real top mass. The advantage of this method is that it has a relatively clear mass definition (the non-perturbative effects are still inevitable), but the accuracy is not so good.

Current PDG values are [1]:

Direct measurement

$$m{=}173.1{\pm}0.6\ \text{GeV},$$

$\overline{\rm MS}$ mass from cross section measurements

$$m{=}160^{+5}_{-4}\ \text{GeV},$$

Pole mass from cross section measurements

$$m{=}173.5{\pm}1.1\ \text{GeV}.$$

Alternatively, there is a third method which uses a top pair threshold scan at future 350 GeV $\rm e^+e^-$ colliders, e.g. the International Linear Collider (ILC), the Compact Linear Collider (CLIC), the $\rm e^+e^-$ Future Circular Collider (FCC-ee), CEPC, and so on. The corresponding simulations have been performed in Refs. [14–16]. Because of the clear mass definition, sensitive dependence of the cross section on the top mass and low background pollution, this method is believed to be the best choice to obtain the most accurate top mass, although it is expensive and time consuming.

This paper is organized as follows. In Section 2, we review the framework of threshold top pair production cross section, which has been calculated up to NNNLO QCD level. In Section 3, we perform Poisson sampling and χ^2 fitting by using `Minuit` [17] code, and present an equivalent error matrix analysis for the statistical uncertainty estimation. In Section 4, we discuss briefly the impact of future CEPC top mass measurement on the electroweak vacuum stability. In Section 5, we give a short summary.

2 Cross section

The theoretical higher order QCD calculations of the cross section $\rm e^+e^- \to \gamma^*/Z^* \to t\bar{t}$ near threshold are built in the framework of nonrelativistic quantum chromodynamics (NRQCD) [18, 19] and potential nonrelativistic quantum chromodynamics (pNRQCD) [20]. NRQCD is obtained by integrating out the hard part $\mathcal{O}(m)$ of the QCD and pNRQCD is obtained by integrating out the soft part $\mathcal{O}(mv)$ of NRQCD. The top pair production cross section at NNLO was first calculated in the 1990s, e.g. Ref. [8], and has recently been updated to NNNLO QCD [21]. However, when the energy approaches the threshold, the top quark velocity v becomes very small. The corresponding resummation for Coulomb singularities and large logarithms is obtained at next-to-leading-logarithmic order (NLL) [22] and known partially at next-to-next-to-leading-logarithmic order (NNLL) as shown in Refs. [23–26]. However, as argued in Ref. [27], the NNLL QCD prediction can still be employed, because the missing mixing corrections from soft and potential NLL RG evolution of non-Coulomb QCD potential are very likely negligible. These are implemented in the Monte Carlo generator `Whizard` [28], which can produce multi-particle process simulations at $\rm e^+e^-$ colliders. It includes a model "SM_tt_threshold.mdl " that can be used to calculate the top pair production cross section near the threshold at LL order and NLL order [29–31]. Because top quark pairs are unstable and decay to $\rm W^+W^-b\bar{b}$ instantaneously when they are produced, the full process $\rm e^+e^- \to W^+W^-b\bar{b}$ should be taken into account, thus it has backgrounds which come from the decay of $\rm W^+W^-$, ZZ and ZH etc. As pointed out in Ref. [32], these backgrounds can increase the total cross section. In order to reduce these backgrounds, invariant mass cuts for $\rm W^+b$ and $\rm W^-\bar{b}$ are needed and can take the form $|M_{\rm W,b}{-}m_{\rm t}|{\leqslant}\triangle M_{\rm t}$. The analysis in Ref. [33] shows that a cut with $\triangle M_{\rm t} \backsim 15$ – 35 GeV is moderate, so in our calculations we set $\triangle M_{\rm t} = 30$ GeV.

In the following, we briefly review the theoretical framework of the total cross section calculations for the top pair bound state. The top pair total cross section can be written in the form

$$\sigma(\rm e^+e^- \to t\bar{t}{+}X){=}\sigma_0{\cdot}(R^v{+}R^a), \tag{16}$$

where $\sigma_0 = 4\pi\alpha^2/3s$ is the cross section for the $\mu^+\mu^-$

pair at tree level, with $s=q^2=(E+2m_{\rm t})^2$ is the square of center-of-mass energy, and R^v and R^a are the ratios contributed by vector current and axial-vector current respectively. These can be related to the two-point functions of the vector current and the axial-vector current separately by the optical theorem,

$$\begin{aligned}R^v=&\left[\left(e_{\rm t}-\frac{q^2v_{\rm e}v_{\rm t}}{q^2-m_{\rm Z}^2}\right)^2+(\frac{q^2}{q^2-m_{\rm Z}^2})^2\cdot a_{\rm e}^2v_{\rm e}^2\right]\mathcal{I}m(\Pi^v(q^2)),\\ R^a=&\left(\frac{q^2}{q^2-m_{\rm Z}^2}\right)^2(v_{\rm e}^2+a_{\rm e}^2)a_{\rm t}^2\mathcal{I}m(\Pi^a(q^2)),\end{aligned}\tag{17}$$

where the vector and axial-vector couplings of fermions to the Z boson are

$$v_{\rm f}=\frac{T_3^{\rm f}-2e_{\rm f}\sin^2\theta_{\rm w}}{2\sin\theta_{\rm w}\cos\theta_{\rm w}},\quad a_{\rm f}=\frac{T_3^{\rm f}}{2\sin\theta_{\rm w}\cos\theta_{\rm w}},\tag{18}$$

with $e_{\rm f}$ the electric charge of the fermion in units of positron charge ($e_{\rm f}=2/3$ for top quark and $e_{\rm f}=1$ for electron), $T_3^{\rm f}$ is the third component of its weak isospin, and $\theta_{\rm w}$ denotes the Weinberg angle.

The two-point Green function of vector (or axial-vector) current is given by [34]

$$\begin{aligned}\Pi_{\mu\nu}^X=&i\int{\rm d}^4x{\rm e}^{iq\cdot x}\langle0|Tj_\mu^X(x)j_\nu^X(0)|0\rangle\\ =&(q_\mu q_\nu-q^2g_{\mu\nu})\Pi^X(q^2)+q_\mu q_\nu\Pi_L^X(q^2),\end{aligned}\tag{19}$$

where $X=v$ (or $X=a$) denotes the vector (or axial-vector) current, and $j_\mu^X=\bar{t}\gamma_\mu t$ (or $\bar{t}\gamma_\mu\gamma_5 t$).

In the framework of (p) NRQCD, the expansion of the vector and axial-vector currents read

$$\begin{aligned}j_k^v=&c_v\psi^\dagger\sigma_k\chi+\frac{d_v}{6m_{\rm t}^2}\psi^\dagger\sigma_k\boldsymbol{D}^2\chi+...,\\ j_k^a=&\frac{c_a}{2m_{\rm t}}\psi^\dagger[\sigma_k,(-i)\vec{\sigma}\cdot\boldsymbol{D}]\chi+...,\end{aligned}\tag{20}$$

where σ_k is the Pauli matrix and $\boldsymbol{D}=-\vec{\bigtriangledown}$, ψ is the top quark field and χ is the anti-top quark field, and c_v, d_v and c_a are the non-relativistic QCD (NRQCD) matching coefficients of vector and axial-vector currents [34, 35]. In the center-of-mass frame (CM frame), the momentum $q^\mu=(q^0,\boldsymbol{0})=(E+2m_{\rm t},\boldsymbol{0})$. From Eq. (19), one can easily rewrite Eq. (17) in d-dimensional space, and

$$\begin{aligned}R^v=&\frac{1}{(d-1)q^2}\left[\left(e_{\rm t}-\frac{q^2v_{\rm e}v_{\rm t}}{q^2-m_{\rm Z}^2}\right)^2+\left(\frac{q^2}{q^2-m_{\rm Z}^2}\right)^2\cdot a_{\rm e}^2v_{\rm e}^2\right]\\ &\times\mathcal{I}m(i\int{\rm d}^4x{\rm e}^{iq^0\cdot x^0}\langle0|Tj_k^X(x)j_k^X(0)|0\rangle),\\ R^a=&\frac{1}{(d-1)q^2}\left(\frac{q^2}{q^2-m_{\rm Z}^2}\right)^2(v_{\rm e}^2+a_{\rm e}^2)a_{\rm t}^2\\ &\times\mathcal{I}m\left(i\int{\rm d}^4x{\rm e}^{iq^0\cdot x^0}\langle0|Tj_k^X(x)j_k^X(0)|0\rangle\right).\end{aligned}\tag{21}$$

By inserting Eq. (20) into Eq. (21) and making the following substitutions

$$\begin{aligned}G^S(E)=&\frac{i}{2N_c(d-1)}\int{\rm d}^4x{\rm e}^{iEx^0}\langle0|T(\chi^\dagger\sigma_k\psi)(x)(\psi^\dagger\sigma_k\chi)(0)|0\rangle,\\ G^P(E)=&\frac{i}{2N_c}\int{\rm d}^4x{\rm e}^{iEx^0}\langle0|T(\chi^\dagger iD_k\psi)(x)(\psi^\dagger iD_k\chi)(0)|0\rangle,\end{aligned}\tag{22}$$

where the superscripts "S" and "P" denote the S-wave state and the P-wave state respectively, the R^v and R^a are simplified to

$$\begin{aligned}R^v=&\left[\left(e_{\rm t}-\frac{q^2v_{\rm e}v_{\rm t}}{q^2-m_{\rm Z}^2}\right)^2+\left(\frac{q^2}{q^2-m_{\rm Z}^2}\right)^2\cdot a_{\rm e}^2v_{\rm e}^2\right]\\ &\cdot\frac{N_c}{2m_{\rm t}^2}c_v\left[c_v-\frac{E}{m_{\rm t}}\left(c_v+\frac{d_v}{3}\right)\right]\mathcal{I}m\{G^S(E)\},\\ R^a=&(\frac{q^2}{q^2-m_{\rm Z}^2})^2(v_{\rm e}^2+a_{\rm e}^2)a_{\rm t}^2\cdot\frac{N_cc_a^2}{2m_{\rm t}^4}\frac{d-2}{d-1}\mathcal{I}m\{G^P(E)\}.\end{aligned}\tag{23}$$

In (p)NRQCD perturbation theory, the expansion for the Green function $G^S(q^0)$ takes

$$G^X(E)=G_0^X(E)+\sum_{i=1}^n\delta_iG^X(E),\tag{24}$$

where $G_0^X(E)=G_0^X(0,0;E)$ is the zero-point Green function in coordinate space, which can be derived by solving the non-relativistic Schrödinger equation in spherical coordinates,

$$\left[-\frac{1}{m_{\rm t}}\left(\frac{{\rm d}^2}{{\rm d}r^2}+\frac{2}{r}\frac{\rm d}{{\rm d}r}\right)-\frac{C_{\rm F}\alpha_{\rm s}}{r}-E\right]G_0(\boldsymbol{r},\boldsymbol{r}';E)=\frac{1}{4\pi r^2}\delta(\boldsymbol{r}-\boldsymbol{r}').\tag{25}$$

$\delta_iG^X(E)(i=1,2,3,...)$ are the higher order corrections, which are not only related to the higher order corrections of the Coulomb potential but also $G_0^X(E)$. The complete S-wave $G^X(E)=G^S(E)$ calculations at third order are provided in Ref. [35] and the P-wave $G^X(E)=G^P(E)$ at the same order is included in Ref. [34]. The complete numerical calculations are implemented in the `QQbar_threshold` code [36].

The experimentally observed cross section is calculated by convoluting the theoretical cross section with the initial state radiation (ISR) factor and the luminosity spectrum (LS),

$$\sigma_{\rm t\bar{t}}^{\rm obs}(\sqrt{s})=\int_0^\infty{\rm d}\sqrt{s'}G(\sqrt{s'},\sqrt{s})\int_0^1{\rm d}xF(x,s')\sigma_{\rm t\bar{t}}^{\rm th}(\sqrt{s'}(1-x)),\tag{26}$$

where $\mathrm{G}(\sqrt{s'},\sqrt{s})$ is the correction function due to large energy spread mainly caused by beamstrahlung and synchrotron radiation [37, 38], which is usually described by a Gaussian function at circular colliders [39], $F(x,s')$ is the initial state radiation factor [40], and $\sigma_{\rm t\bar{t}}^{\rm th}(\sqrt{s'}(1-x))$ is the theoretical cross section at NNNLO QCD order computed by `QQbar_threshold` code. In Fig. 1, the red curve is the purely QCD calculation of total cross section

at NNNLO order. The so-called top pair bound state can be clearly seen just above the threshold energy point. The blue and green curves are the total cross sections corrected by luminosity spectrum (LS) and ISR respectively. The black curve corresponds to the observed total cross section. We see that the ISR correction observably decreases the total cross section.

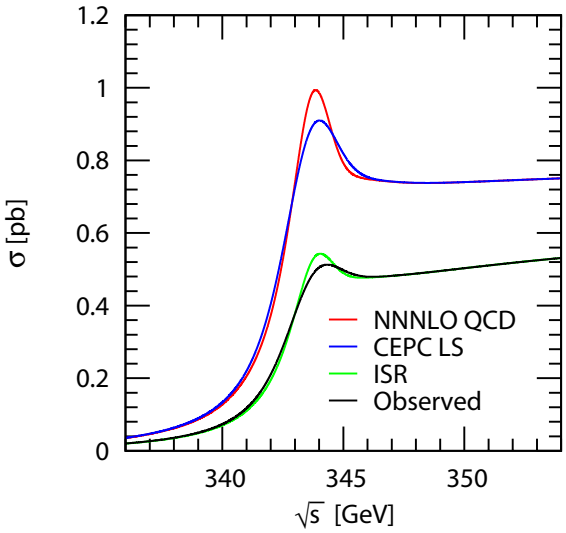

Fig. 1. (color online) The red curve corresponds to the theoretical cross section at NNNLO QCD order obtained by the `QQbar_threshold` code. The blue curve includes the luminosity spectrum (LS) correction at the CEPC. The green curve adds the impact from the initial state radiation (ISR) correction, and the black curve is the experimentally observed cross section.

To simulate a top mass threshold scan experiment, we should assume an attempt top mass value as an initial input parameter. The locations of the optimal energy points, which are determined by the simulation, may vary when the real top mass is different from our assumed value. However, the optimization method itself will not change. We will discuss this problem after the simulation.

In our calculation, we adopt the PS mass scheme and our input parameters are set the same as in Ref. [21]; $m_{\rm t}{}^{\rm PS}(\mu_{\rm f}=20\ {\rm GeV})=171.5\ {\rm GeV}$, and $\Gamma_{\rm t}=1.33\ {\rm GeV}$. Other input parameters are set as the default values in the `QQbar_threshold` code. We set an approximate value for the energy spread of 0.1629%, which is the designed energy spread at 240 GeV center-of-mass energy at CEPC [37–39] and which we estimate will not change much in the $\rm t\bar{t}$ threshold region.

3 Top mass measurement scheme

First, the experimental top mass measurements are simulated by using the software `Minuit` to perform the χ^2 fittings. The number of optimal energy points and their locations are determined. Second, a substitutable theoretical analysis on the statistical error matrix in a one-point scheme is provided, which can calculate the statistical error directly even without any data-sampling and fitting. Finally, the luminosity dependence of the top mass statistical error is analysed and the accuracy of the top mass that can be achieved at the future collider CEPC is discussed.

The crucial problem for a top mass threshold measurement optimization is to determine the number of energy points to be taken and their locations. Actually, related studies [14–16] have already been made to simulate the threshold scan at future $\rm e^+e^-$ colliders. In these studies, the data taking schemes are usually designed as 10 equal-distance energy points in a selected near-threshold energy region with equal luminosity distributed on each energy point. It is easy to imagine that these 10 points definitely will not contribute equally to the fitted top mass, due to their different sensitivity to the variations of the top mass and cross sections. In fact, it has been shown [41] in the case of a similar tau lepton mass threshold scan that the most efficient scheme is to concentrate all luminosity on a single optimal energy point in one free mass parameter fitting (sometimes the background cross section and the selection efficiency can also be taken as free parameters to be fitted, which is called multi-parameter fitting, and which we do not consider here). We have checked this result and find that the additional energy points far from the optimal energy point have a negligible contribution to minimizing the statistical error of the fitted top mass, and this indicates that they are completely unnecessary.

To find the location of the single optimal energy point, we perform several χ^2 fittings in the one energy point scheme, with the single energy point ranging from 342 GeV to 346 GeV with a step size of 0.1 GeV. The general χ^2 function takes the form:

$$\chi^2=\sum_{i=1}^{n}\frac{[N_i-\mu_i(m_{\rm t})]^2}{\mu_i(m_{\rm t})}, \tag{27}$$

where n is the number of energy points ($n=1$ in the single energy point case), and N_i is the number of top pair events simulated by Poisson sampling according to the Poisson expectation value $\mu_i(m_{\rm t})$ of the ith energy point. One may bring the criticism that a real simulation should include event generation, signal selection, and background estimation. However, we emphasize that this simplified simulation has already demonstrate the stochastic behavior in top pair production and the optimization result will not change. A simulation based on Monte Carlo event generators is being analyzed and will

be reported elsewhere. μ_i is given by

$$\mu_i=[\epsilon_{\rm sig}\cdot Br_{\rm Wb}\cdot\sigma^{\rm obs}_{\rm t\bar{t}}(\sqrt{s_i},m_{\rm t})+\sigma_{\rm BG}]\cdot\mathscr{L}_i \sim\mathscr{L}^i_{\rm eff}\cdot Br_{\rm Wb}\cdot\sigma^{\rm obs}_{\rm t\bar{t}}(\sqrt{s_i},m_{\rm t}), \quad (28)$$

where $\epsilon_{\rm sig}$ is the top pair selection efficiency; $Br_{\rm Wb}$ is the branching ratio for the decays of $t\to W^+b$ and $\bar{t}\to W^-\bar{b}$, and we set $Br_{\rm Wb}=1$; $\sigma^{\rm obs}_{\rm t\bar{t}}(\sqrt{s_i},m_{\rm t})$ can be obtained from Eq. (26); $\sigma_{\rm BG}$ is the background cross section; and $\mathscr{L}^i_{\rm eff}=\mathscr{L}_i\cdot\epsilon_{\rm sig}$ is the effective luminosity for the ith energy point. Most of the backgrounds can be reduced by the invariant mass cut, as discussed in Section **2**. Background can also be suppressed by other selection cuts [42]. The interference between the resonant top pair decay and the single top decay process is also suppressed by v^2 [43], with v being the top quark velocity. Therefore, the backgrounds can safely be neglected in such a clean experiment.

Generally speaking, the observable cross section $\sigma^{\rm obs}_{\rm t\bar{t}}$ has two variable parameters, the top quark PS mass $m_{\rm t}$ and the ECM $\sqrt{s}$. The change of the top quark width, as well as the strong coupling constant due to the variation of $m_{\rm t}$ and $\sqrt{s}$, can be neglected. For convenience of the numerical calculations, the shape of the cross section can be approximately taken as stable and the change of $m_{\rm t}$ can only cause a horizontal shift along the energy axis. Thus, the two variables $m_{\rm t}$ and $\sqrt{s}$ can be reduced to a single one $\sqrt{s}$ - $2\Delta m_{\rm t}$ as

$$\sigma^{\rm obs}_{\rm t\bar{t}}(\sqrt{s};m_{\rm t})=\sigma^{\rm obs}_{\rm t\bar{t}}(\sqrt{s}-2\Delta m_{\rm t},m_{\rm t0}), \quad (29)$$

where $\Delta m_{\rm t}=m_{\rm t}-m_{\rm t0}$, $m_{\rm t}$ is the top quark PS mass and $m_{\rm t0}=m^{\rm PS}_{\rm t}(\mu_{\rm f}=20\ {\rm GeV})=171.5$ GeV is our initial input parameter.

Besides the χ^2 fitting, the statistical error of the top mass can also be obtained from the error matrix analysis. The covariant matrix is described by

$$V=\frac{\sigma(m_{\rm t};\sqrt{s})}{\mathscr{L}_{\rm eff}}\left[\frac{\partial\sigma(m_{\rm t};\sqrt{s})}{\partial m_{\rm t}}\right]^{-2}. \quad (30)$$

The statistical error is just the square root of the covariance matrix [17],

$$\delta m^{\rm stat.}_{\rm t}=\sqrt{\frac{\sigma(m_{\rm t};\sqrt{s})}{\mathscr{L}_{\rm eff}}}\left[\frac{\partial\sigma(m_{\rm t};\sqrt{s})}{\partial m_{\rm t}}\right]^{-1}. \quad (31)$$

So with Eq. (31) we can calculate the statistical uncertainty directly.

Figure 2 shows the variation of the statistical error of the fitted top mass with different locations of the single energy point to be taken. The red crosses are our fitted results from `Minuit` with fixed $\mathscr{L}_{\rm eff}=5$ fb^{-1} at each energy point for each fitting. The black curve is the corresponding statistical uncertainty from the analytic calculation of error matrix by Eq. (31). A point "A" at $\sqrt{s}\simeq342.6$ GeV is found to be the optimal energy point. This point is located near but not exactly on the largest slope of the plot of total cross section against $\sqrt{s}$ in Fig. 3, as there is a $\sqrt{s}$ dependent term in front of the derivative shown in Eq. (31). From the figure, the statistical uncertainties from the analytic calculation agree well with those from the χ^2 fitting in region $\sqrt{s}\in[342.0,344.0]$ GeV, but the consistency is not so good when the energy points approach or go above the threshold. This is due to the tiny value of the slope of the cross section here, as shown in Fig. 3. Neither the χ^2 fitting by `Minuit` nor the error matrix analysis have rapid convergence in this region and this indicates that it is a waste of luminosity to take energy points in this small slope region.

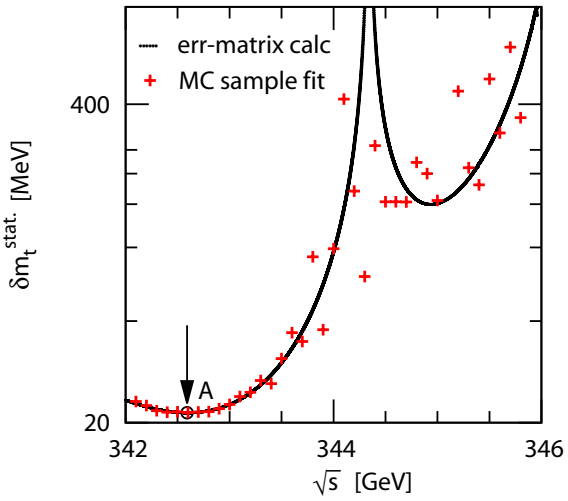

Fig. 2. (color online) The relation between the statistical error $\delta m_{\rm t}$ and the location of the single data-taking energy point along the $\sqrt{s}$-axis. The black curve is calculated by Eq. (31) from the error matrix with fixed $\mathscr{L}_{\rm eff}=5$ fb^{-1}, and the red crosses correspond to the χ^2 fitted results.

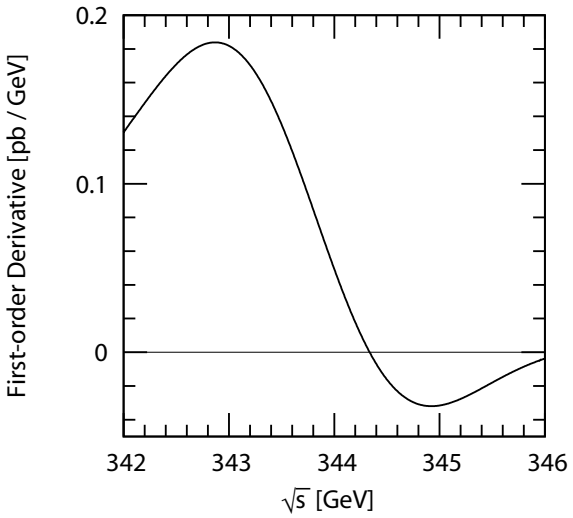

Fig. 3. The first order derivative of the total cross section with respect to the energy.

Figure 4 shows the decrease of the statistical uncertainty as $\mathscr{L}_{\rm eff}$ increases at the fixed optimal point $\sqrt{s}$=342.6 GeV. The red curve corresponds to statistical uncertainty from analytic calculation of the error matrix and the black dots are fitted results from `Minuit`. Both of them coincide with each other. When $\mathscr{L}_{\rm eff}=50$ fb^{-1}, the statistical uncertainty is $\delta m_{\rm t}^{\rm stat.}=7$ MeV. Higher luminosity will not result in a significant decrease of the statistical error.

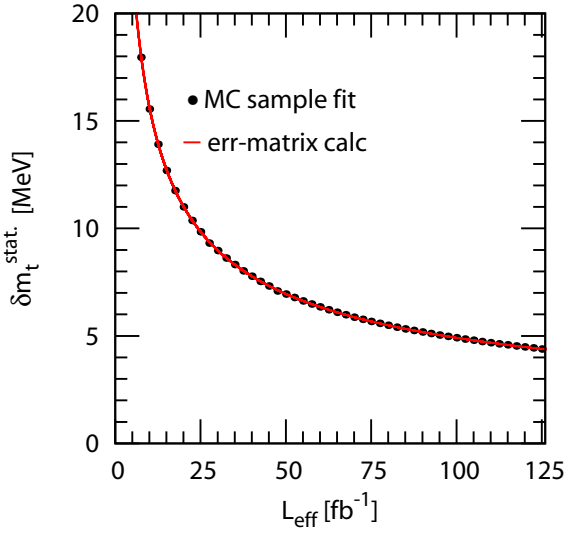

Fig. 4. (color online) The correlation between the statistical error $\delta m_{\rm t}^{\rm stat.}$ and the $\mathscr{L}_{\rm eff}$ in the optimal one-point $\sqrt{s}$=342.6 GeV scheme. The black dots are χ^2 fitted points, and the red curve is computed from error matrix analysis.

The theoretical uncertainty of the normalized total cross section at NNNLO QCD order is estimated at 3% [21]. In our analysis, we assumed that the variation of top mass depends linearly on the total cross section, then the theoretical error of the top mass can be derived by the error transmission formula,

$$\delta m_{\rm t}^{\rm theory}=\delta\sigma(m_{\rm t},\sqrt{s})\cdot\left[\frac{\partial\sigma(m_{\rm t},\sqrt{s})}{\partial m_{\rm t}}\right]^{-1}. \quad (32)$$

Substituting the approximate formula $\partial\sigma(m_{\rm t};\sqrt{s})/\partial m_{\rm t}=2\partial\sigma(m_{\rm t};\sqrt{s})/\partial\sqrt{s}$ into Eq. (32), the top mass theoretical uncertainty is extracted to be $\pm$ 25.6 MeV, which is significantly larger than the statistical uncertainty. A similar result has previously been presented in Ref. [16]. For systematic uncertainty, simulation studies show it is expected to be about 10 MeV at FCC-ee [44]. Without a careful analysis, which depends on detailed information about the hardware, we expect here an equal value of the systematic error at CEPC. Thus, the total accuracy of the PS top mass that can be measured at CEPC is estimated at about $\delta m_{\rm t}^{\rm total}\sim$30 MeV, in which the statistical and systematic errors are comparable and the theoretical error is the dominant source.

Considering a real experiment, the situation is somewhat different from our simulation, as the initial input top mass is not necessarily equal to the real top mass. The solution is to iterate the fitting until it reaches an acceptable accuracy. This means we put in an initial top mass and find the corresponding single optimal energy point location, accumulate some events here, do the fitting and get a measured top mass. Then we take this experimentally measured top mass as input parameter to determine the new location of the single optimal energy point, take data, and do the fitting again. The iteration can be stopped when the statistical uncertainty is suppressed to an acceptable accuracy. So, the single optimal energy point does not mean we only take data at one energy point in the whole experiment, but one energy point in each fitting. The fitting itself can be done many times. This iterative technique is the so called "data-driven" method.

In order to compare the different point selection schemes, we also perform a 10 point scheme as employed in the simulations in Refs. [15, 16]. We take energy points from 340 GeV to 349 GeV in steps of 1 GeV and assign an average of 5 fb^{-1} effective integrated luminosity for each point. The total effective 50 fb^{-1} integrated luminosity results in about 15 MeV statistical uncertainty, which is similar to the results in Refs. [15, 16]. In comparison, the one point scheme leads to a sizeable improvement, about 50% decrease in the top mass statistical uncertainty.

4 Impact of accurate top mass on electroweak vacuum stability

The sensitivity of the electroweak vacuum stability to the top mass is usually calculated in the pole mass scheme. The reason is that currently the most precise value is the directly measured top mass from hadron colliders. In principle, one could also use the short distance masses, such as the PS or $\overline{\rm MS}$ mass directly obtained from the future e^+e^- collider, in the study of vacuum stability, as long as a self-consistent mass definition and renormalization scheme is adopted. Thus, the ambiguity of the pole mass can be avoided. Recent discussions on the pole mass ambiguity can be found in Refs. [45, 46].

Different theoretical defined top masses can be converted from each other. For example, Ref. [47] discussed the relation between $\overline{\rm MS}$ and the pole mass. Here we show the conversion from the PS mass taken in our simulation to the pole mass. The relation between the PS top mass and the pole mass with corrections up to NNNLO QCD order takes the form [48],

$$m_{\rm t}{}^{\rm pole}=m_{\rm t}{}^{\rm PS}(\mu_{\rm f})+\frac{\mu_{\rm f}C_{\rm F}\alpha_{\rm s}(\mu)}{\pi}\left[1+\frac{\alpha_{\rm s}(\mu)}{4\pi}(2\beta_0 l_1+a_1)+\left(\frac{\alpha_{\rm s}(\mu)}{4\pi}\right)^2(4\beta_0^2 l_2+2(2a_1\beta_0+\beta_1)l_1+a_2)\right.$$
$$\left.+\left(\frac{\alpha_{\rm s}(\mu)}{4\pi}\right)^3\left(8\beta_0^3 l_3+4\left(3a_1\beta_0^2+\frac{5}{2}\beta_0\beta_1\right)l_2+2(3a_2\beta_0+2a_1\beta_1+\beta_2)l_1+a_3+16\pi^2 C_{\rm A}^3\right)\right], \quad (33)$$

where $C_{\rm F}=4/3$, $C_{\rm A}=3$, $l_1=\ln(\mu/\mu_{\rm f})+1$, $l_2=\ln^2(\mu/\mu_{\rm f})+2\ln(\mu/\mu_{\rm f})+2$, $l_3=\ln^3(\mu/\mu_{\rm f})+3\ln^2(\mu/\mu_{\rm f})+6\ln(\mu/\mu_{\rm f})+6$, $\mu_{\rm f}$ is the subtraction scale and we set $\mu_{\rm f}=20$ GeV for consistency with setting $m_{\rm t}{}^{\rm PS}(\mu_{\rm f}=20\ {\rm GeV})=171.5$ GeV, μ is the renormalization scale as mentioned above and we set $\mu=80$ GeV, β_0, β_1, β_2 are the renormalization QCD β-functions calculated in [49], and a_1, a_2, a_3 are constant coefficients related to the color factors and the number of light quarks, as given in Refs. [48, 50].

The top pole mass reads

$$m_{\rm t}^{\rm pole}=173.294\pm0.007({\rm stat.})\pm0.026({\rm theory})\pm\mathcal{O}(0.2)({\rm ambiguity})\ {\rm GeV}, \quad (34)$$

where the three-loop strong running coupling [51] has been used. Obviously, the uncertainty of the top pole mass is dominated by the intrinsic ambiguity, which is estimated to be $\mathcal{O}(200)$ MeV [4]. Neither experimental efforts nor higher order theoretical calculations can contribute to reduce this intrinsic uncertainty.

As far as studies of vacuum stability at colliders are concerned, the LHC could extract the Higgs boson mass with an accuracy of $\mathcal{O}(200)$ MeV [1] and top quark pole mass with an accuracy of $\mathcal{O}(1)$ GeV [52], as concluded in Ref. [53]. The stable vacuum can be excluded at 98% confidence level (C.L.) and only a small stable vacuum region is left in the $[m_{\rm h},m_{\rm t}^{\rm pole}]$ contour. At the future ILC, the top quark pole mass is estimated with an accuracy of 200 MeV and uncertainties of the Higgs boson are assumed to be below 50 MeV. A metastable vacuum in the Standard Model is expected at 95% C.L. [54]. At the future CEPC, the Higgs boson mass can be extracted with an experimental accuracy of $\mathcal{O}(10)$ MeV [55]. Our research here shows that at CEPC, the uncertainty of the top short distance mass is about 30 MeV. It is hopeful that the precision of the vacuum stability will be highly improved by using the more accurate short distance top mass obtained from the future lepton colliders.

5 Summary

In this paper, a threshold scan of a top quark mass measurement experiment at a future e^+e^- collider near 350 GeV has been simulated, and the data taking strategy optimized to minimize the statistical fluctuation of the top mass. The top pair production cross section adopted is up to NNNLO QCD level and the potential subtracted top mass is selected, as it is free from the intrinsic ambiguity in the pole mass definition. The optimization shows that there should be only one energy point, located near the largest slope region of the plot of cross section against beam energy. The result has been checked by error matrix calculation of the statistical error. The so called data-driven method could be the best choice for future real top mass measurement experiments, which means the fitted top mass should be taken as a new input parameter to determine the next location of the optimal energy point, with this iterative fitting stopped when the statistical error is minimized to an acceptable value. Our research has already shown the advantage of this optimized scheme. As data events are recorded at the most efficient single energy point, 7 MeV statistical uncertainty can be achieved within 50 $\rm fb^{-1}$ effective integrated luminosity, which is about half the uncertainty of the 10 average distributed points scheme used in Refs. [15, 16] with an equal total integrated luminosity.

The 3% theoretical uncertainty for the normalized top pair production cross section caused by the renormalization scale variation leads to a 25.6 MeV theoretical uncertainty for the top mass. Although a hardware-dependent systematic uncertainty analysis is still absent here, our simulation shows that the systematic error at the future CEPC is expected to be comparable to the statistical uncertainty at about $\mathcal{O}(10)$ MeV, the same as at the FCC-ee [44]. Actually, short distance top masses, which could be accurately determined from a threshold scan in the future 350 GeV lepton colliders, can be adopted directly in the vacuum stability calculation. Together with the precise Higgs mass measured at a future e^+e^- 250 GeV collider, it is sufficient to make a final conclusion of the fate of the Standard Model electroweak vacuum stability. It is hard to imagine that a metastable vacuum is just coincidental, and undiscovered new physics is highly expected.

References

1 Particle Data Group, C. Patrignani et al, Chin. Phys. C, **40**: 100001 (2016)
2 A. H. Hoang, M. C. Smith, T. Stelzer, and S. Willenbrock, Phys. Rev. D, **59**: 114014 (1999), arXiv:hep-ph/9804227
3 M. C. Smith and S. S. Willenbrock, Phys. Rev. Lett., **79**: 3825 (1997), arXiv:hep-ph/9612329
4 M. Beneke and V. M. Braun, Nucl. Phys. B, **426**: 301 (1994), arXiv:hep-ph/9402364
5 P. Nason, arXiv:1712.02796

6 M. Beneke, Phys. Lett. B, **434**: 115 (1998), arXiv:hep-ph/9804241
7 Y. Kiyo and Y. Sumino, Phys. Rev. D, **67**: 071501 (2003), arXiv:hep-ph/0211299
8 A. H. Hoang and T. Teubner, Phys. Rev. D, **58**: 114023 (1998), arXiv:hep-ph/9801397
9 U. Husemann, Prog. Part. Nucl. Phys., **95**: 48 (2017), arXiv:1704.01356
10 J. Fuster, A. Irles, D. Melini, P. Uwer, and M. Vos, (2017), arXiv:1704.00540
11 G. Cortiana, Rev. Phys., **1**: 60 (2016), arXiv:1510.04483
12 CMS, S. Chatrchyan et al, Phys. Lett. B, **728**: 496 (2014), arXiv:1307.1907; Phys. Lett.B, **738**: 526 (2014)
13 D0, V. M. Abazov et al, Phys. Lett., **B703**: 422 (2011), arXiv:1104.2887.
14 M. Martinez and R. Miquel, Eur. Phys. J. C, **27**: 49 (2003), arXiv:hep-ph/0207315
15 K. Seidel, F. Simon, M. Tesar, and S. Poss, Eur. Phys. J. C, **73**: 2530 (2013), arXiv:1303.3758
16 F. Simon, PoS, **ICHEP2016**: 872 (2017), arXiv:1611.03399
17 F. James, Comput. Phys. Commun., **20**: 29 (1980)
18 B. A. Thacker and G. P. Lepage, Phys. Rev. D, **43**: 196 (1991)
19 G. P. Lepage, L. Magnea, C. Nakhleh, U. Magnea, and K. Hornbostel, Phys. Rev. D, **46**: 4052 (1992), arXiv:hep-lat/9205007
20 A. Pineda and J. Soto, Nucl. Phys. Proc. Suppl., **64**: 428 (1998), arXiv:hep-ph/9707481
21 M. Beneke et al, Phys. Rev. Lett., **115**: 192001 (2015), arXiv:1506.06864
22 A. Pineda, Phys. Rev. D, **66**: 054022 (2002), arXiv:hep-ph/0110216
23 A. H. Hoang, A. V. Manohar, I. W. Stewart, and T. Teubner, Phys. Rev. Lett., **86**: 1951 (2001), arXiv:hep-ph/0011254
24 A. H. Hoang, A. V. Manohar, I. W. Stewart, and T. Teubner, Phys. Rev. D, **65**: 014014 (2002), arXiv:hep-ph/0107144
25 A. Pineda, Phys. Rev. D, **65**: 074007 (2002), arXiv:hep-ph/0109117
26 A. Pineda and A. Signer, Nucl. Phys. B, **762**: 67 (2007), arXiv:hep-ph/0607239
27 A. H. Hoang and M. Stahlhofen, JHEP, **1405**: 121 (2014), arXiv:1309.6323
28 W. Kilian, T. Ohl, and J. Reuter, Eur. Phys. J. C, **71**: 1742 (2011), arXiv:0708.4233
29 J. Reuter et al, Top Physics in WHIZARD: in Proceedings, International Workshop on Future Linear Colliders (LCWS15): Whistler, B.C., Canada, November 02-06, 2015, 2016, arXiv:1602.08035
30 J. Reuter et al, PoS, **RADCOR2015**: 088 (2015), arXiv:1601.02459
31 F. Bach and M. Stahlhofen, Top pair threshold production at a linear collider with WHIZARD: in Proceedings, 7th International Workshop on Top Quark Physics (TOP2014): Cannes, France, September 28-October 3, 2014, arXiv:1411.7318
32 A. H. Hoang and M. Stahlhofen, JHEP, **05**: 121 (2014), arXiv:1309.6323
33 A. H. Hoang, C. J. Reisser, and P. Ruiz-Femenia, Phys. Rev. D, **82**: 014005 (2010), arXiv:1002.3223
34 M. Beneke, J. Piclum, and T. Rauh, Nucl. Phys. B, **880**: 414 (2014), arXiv:1312.4792
35 M. Beneke, Y. Kiyo, and K. Schuller, (2013), arXiv:1312.4791
36 M. Beneke, Y. Kiyo, A. Maier, and J. Piclum, Comput. Phys. Commun., **209**: 96 (2016), arXiv:1605.03010
37 X. Mo, G. Li, M.-Q. Ruan, and X.-C. Lou, Chin. Phys. C, **40**: 033001 (2016), arXiv:1505.01008
38 CEPC-SPPC Study Group, CEPC-SPPC Preliminary Conceptual Design Report. 2. Accelerator, 2015
39 M. Koratzinos, CEPC design performance considerations: in Proceedings, 55th ICFA Advanced Beam Dynamics Workshop on High Luminosity Circular e+e- Colliders - Higgs Factory (HF2014): Beijing, China, October 9-12, 2014: p. THT4A2, 2015, arXiv:1501.06854
40 E. A. Kuraev and V. S. Fadin, Sov. J. Nucl. Phys., **41**: 466 (1985), [Yad. Fiz. **41**: 733 (1985)]
41 X. H. Mo, Int. J. Mod. Phys. A, **30**: 1550149 (2015), arXiv:1505.00059
42 T. Horiguchi et al, (2013), arXiv:1310.0563.
43 A. H. Hoang and C. J. Reisser, Phys. Rev. D, **71**: 074022 (2005), arXiv:hep-ph/0412258
44 TLEP Design Study Working Group, M. Bicer et al, JHEP, **01**: 164 (2014), arXiv:1308.6176
45 M. Beneke, P. Marquard, P. Nason, and M. Steinhauser, Phys. Lett. B, **775**: 63 (2017), arXiv:1605.03609
46 A. H. Hoang, C. Lepenik, and M. Preisser, JHEP, **1709**: 099 (2017), arXiv:1706.08526
47 P. Marquard, A. V. Smirnov, V. A. Smirnov, M. Steinhauser, and D. Wellmann, Phys. Rev. D, **94**(7): 074025 (2016) arXiv:1606.06754
48 M. Beneke, Y. Kiyo, and K. Schuller, Nucl. Phys. B, **714**: 67 (2005), arXiv:hep-ph/0501289
49 S. A. Larin and J. A. M. Vermaseren, Phys. Lett. B, **303**: 334 (1993), arXiv:hep-ph/9302208
50 Y. Schroder, Phys. Lett. B, **447**: 321 (1999), arXiv:hep-ph/9812205
51 A. Djouadi, Phys. Rept., **457**: 1 (2008), arXiv:hep-ph/0503172
52 CMS Collaboration, (2012), CMS-PAS-TOP-11-015
53 G. Degrassi et al, JHEP, **08**: 098 (2012), arXiv:1205.6497
54 S. Alekhin, A. Djouadi, and S. Moch, Phys. Lett. B, **716**: 214 (2012), arXiv:1207.0980
55 Z. Chen et al, Chin. Phys. C, **41**: 023003 (2017), arXiv:1601.05352